Contents lists available at ScienceDirect

Heliyon

Research article

The longitudinal and regional analysis of bleomycin-induced pulmonary fibrosis in mice by microcomputed tomography

Ruogu Lai [a], Caiping Zhao [a], Wanyi Guo [a], Yao Xiao [b], Runze Li [b], Liang Liu [a,b,**], Hudan Pan [b,*]

[a] State Key Laboratory of Quality Research in Chinese Medicine, Macau University of Science and Technology, Macau, China
[b] State Key Laboratory of Dampness Syndrome of Chinese Medicine, The Second Affiliated Hospital of Guangzhou University of Chinese Medicine, Guangzhou, 510000, China

ABSTRACT

Introduction: Microcomputed tomography (micro-CT) is powerful for assessment of the progression of lung fibrosis in animal model, but current whole lung analysis (WLA) methods are time-consuming. Here, a longitudinal and regional analysis (LRA) method was developed to assess fibrosis easily and quickly by micro-CT.
Method: Firstly, we investigated the distribution pattern of lesions in BLM-induced pulmonary fibrosis mice. Then, the VOIs for LRA were selected based on the anatomical locations and we compared the robustness, accuracy, repeatability, analysis time of LRA to WLA. Additionally, LRA was applied to assess different stages of pulmonary fibrosis, and was validated with conventional endpoint measurements (such as lung hydroxyproline and histopathology).
Results: The lesions of fibrosis in 66 bleomycin (BLM)-induced pulmonary fibrosis mice were mostly in the middle and upper parts of lungs. By applying LRA, the percentages of high-density voxels in selected volumes of interest (VOIs) were well correlated with that in WLA both at Day 7 and Day 21 after bleomycin induction (R^2 = 0.8784 and 0.8464, respectively). The relative standard deviation (RSD) of the percentage of high-density voxels in the VOIs was lower than that of WLA ($P < 0.05$). The cost time of LRA was shorter than that of WLA ($P < 0.05$) and the accuracy of LRA was further confirmed by the histological analysis and biochemical quantification of hydroxyproline.
Conclusion: LRA is probably an easier and more time-saving method to assess fibrosis formation and evaluate treatment efficacy.

1. Introduction

Idiopathic pulmonary fibrosis (IPF) is a severe and chronic respiratory disorder characterized by permanent fibrotic scarring in the lung tissue, which ultimately leads to progressive respiratory distress [1]. To date, no curative treatment for IPF has been identified [2]. Although increasing preclinical studies conducted for identifying new anti-fibrotic drugs, efficient and accurate measurements for

assessment of fibrosis are still lacking.

Microcomputed tomography (micro-CT) analysis is a useful tool for tracing the progression of lung fibrosis. However, the current methods for quantifying micro-CT images are laborious and time-consuming, and there is a great need for easy and rapid assessment of Micro-CT images for lung diseases. The bleomycin-induced pulmonary fibrosis (BIPF) mouse model has been classically used to simulate human pulmonary fibrosis [3]. Despite the development of micro-CT quantification methods for BIPF mouse models over the past decade [4], this technique has not been routinely employed for monitoring changes in lung fibrosis. Typically, micro-CT is used only at the endpoint of a study [5–8], which makes it challenging to ascertain whether the mice had comparable degrees of fibrosis at the study's start before any therapeutic interventions (no early than 7–10 days post-bleomycin) [9]. This is largely due to the fact that manual tools for micro-CT image analysis are time-consuming and labor-intensive [10]. Hence, developing a straightforward and efficient approach for evaluating the degree of pulmonary fibrosis using micro-CT would be of considerable significance.

In this study, we developed an optimized approach called longitudinal regional analysis (LRA) for the assessment of lung fibrosis. We aimed to validate the robustness, accuracy, repeatability, relative speed of analysis, and minimum requirements of LRA.

2. Methods

2.1. Experimental animals

Prior to model induction, male C57BL/6j mice (12 ± 1 weeks old, 22–30 g) were acclimatized for 7 days to the local vivarium conditions (room temperature: 20–24 °C; relative humidity: 40–70%; 12-h light–dark cycle) with free access to standard rodent chow and reverse–osmosis-filtered water. All procedures were approved by the Animal Ethical Council of Macau University of Science and Technology.

2.2. Establishment of bleomycin induced mice

Mice were anesthetized with 1% pentobarbital sodium intraperitoneally. The dosage was determined by the formula: ($weight$ (g) $\times$ $10 - 120 = amount\ of\ pentobarbital\ sodium\ in\ \mu l$) (eg. C57BL/6 mice in weight of 25 g was administrated with $25\ g \times 10 - 120 = 130\ \mu l$ 1% pentobarbital sodium before Bleomycin administration). BLM (2.0 mg/kg; BLEOCIN, Nippon Kayaku Co., Ltd., Japan)/phosphate-buffered saline (PBS) solution with a volume of 2.0 μl/g was administered intratracheally in 4–5 drops over 2–3 min. For better distribution of BLM, the mice were kept vertical to the ground for 10–15 min after administration. After that, the mice were placed in the supine position until woke up. The same volume of sterile PBS was administered to the control mice. Body weight was tested throughout the experiment.

2.3. In vivo micro-CT imaging

Mice were anesthetized with 1% pentobarbital sodium intraperitoneally. The dosage was determined by the formula: $mouse's\ weight$ ($weight$ (g) $\times$ $10 - 100 = amount\ of\ pentobarbital\ sodium\ in\ \mu l$) (eg. C57BL/6 mice in weight of 25 g was administrated with $25\ g \times 10 - 100 = 150\ \mu l$ 1% pentobarbital sodium before micro-CT scanning). The respiration rate was set as 1.2–1.4/s, monitored by the physiological monitoring module of Skyscan 1076 (Brucker). To maintain the shape of the lung as consistent as possible, anesthetized mice were set in the supine position, and the limbs were fixed to exact positions with markers placed in the cabin. Images were acquired in list-mode with the following parameters: 65 kVp X-ray source voltage, 300μA current, a composite X-ray filter of 1.0 mm aluminum, 120 ms camera exposure time per projection, 4 projections per view, 23 × 35 mm field of view, acquiring projections with 0.5-degree increments over a total angle of 180°, producing images with a pixel size of 16.8 μm. Tomograms were reconstructed using Nrecon software (version 1.6.1.3, SkyScan, Burcker). Reconstruction parameters were smoothing "1", beam-hardening correction "0%'', ring artifact correction "10%", region of interest (ROI) "cycle". To export BMP images with appropriate contrast for image analysis, HU units were converted to gray values between 0 and 0.0255 using the HU units-gray value mapping table. Subsequently, gray values were reconverted to HU units to reflect the tissue density. The sagittal plane of the mice was corrected to vertical before image reconstruction. The reconstructed 3D datasets had an isotropic 16.8 μm voxel size and a 1000 × 1000 voxel size for the region of interest.

2.4. Semi quantification analysis

The average percentage of fibrotic area in six specific levels was scored by Hyun Ju Lee Semi quantification analysis Scoring system [4]. Briefly, Ground-glass opacity (GGO), consolidation, parenchymal lines were scored in 6 levels in each side of lung on micro-CT images, and honeycombing, and peripheral bronchial dilatation were scored were scored in 3 levels. The semi-quantitative scoring of the sections was performed by an operator blinded to the treatment.
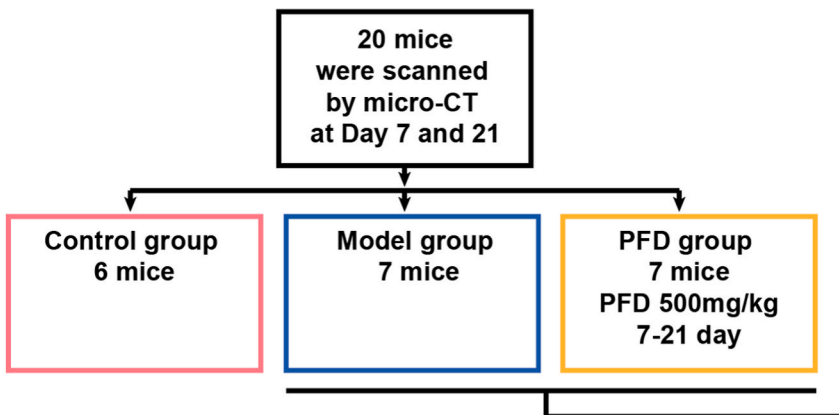
2.5. Longitudinal and regional analysis (LRA)

To investigate the distribution pattern of pulmonary fibrosis lesions in BLM-induced pulmonary fibrosis (BIPF) mice, a total of 66 model mice were scanned at Day 21 post-instillation. After acquisition of micro-CT images, semi-quantification scoring was used to
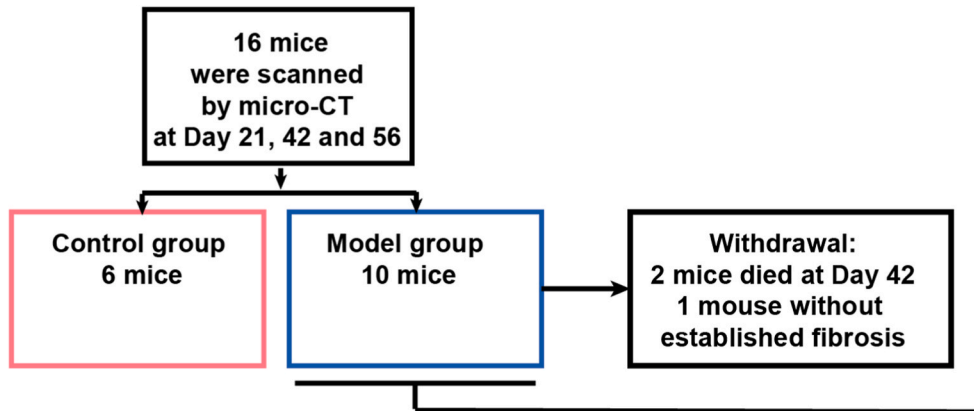
Part 1. Method optimization
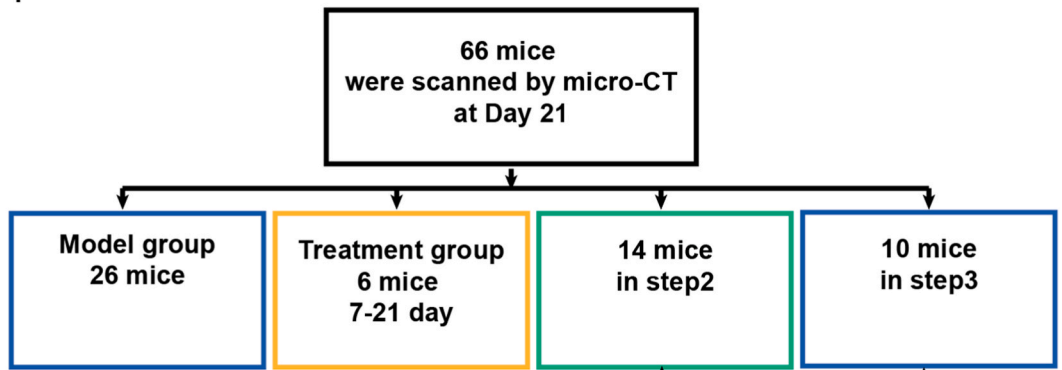
Fig. 1. Illustration of involved mice in each phase.

calculated and detect the susceptible site of fibrosis where is most likely to happen pulmonary fibrosis in BLM mouse models. The process of Longitudinal and regional analysis (LRA) was consisted of five steps: in vivo micro-CT imaging with fixed posture, image reconstruction, subvolume extraction, histogram analysis, and comparison before or after treatment. Three points in the upper and middle parts of the mouse's lung are selected and labeled A, B, and C. The first point (A) is located at the fork where the right main bronchus (RMB) splits into the cranial right main bronchus (CrRMB); the second point (B) is at the fork where the RMB splits into the middle right main bronchus (MiRMB); and the third point (C) is at the fork where the left main bronchus (LMB) splits into the second left branch bronchus (the first branch bronchus divides outside the lung). The three spots (A, B, C) were designated by the intersection of the horizontal plane (blue line, slice Z), coronal plane (green line, slice Y), and sagittal plane (red line, slice X) in the orthographic projection of the mouse. These intersections can be viewed from the top, front, and side perspectives. Next, cubic volumes of interest
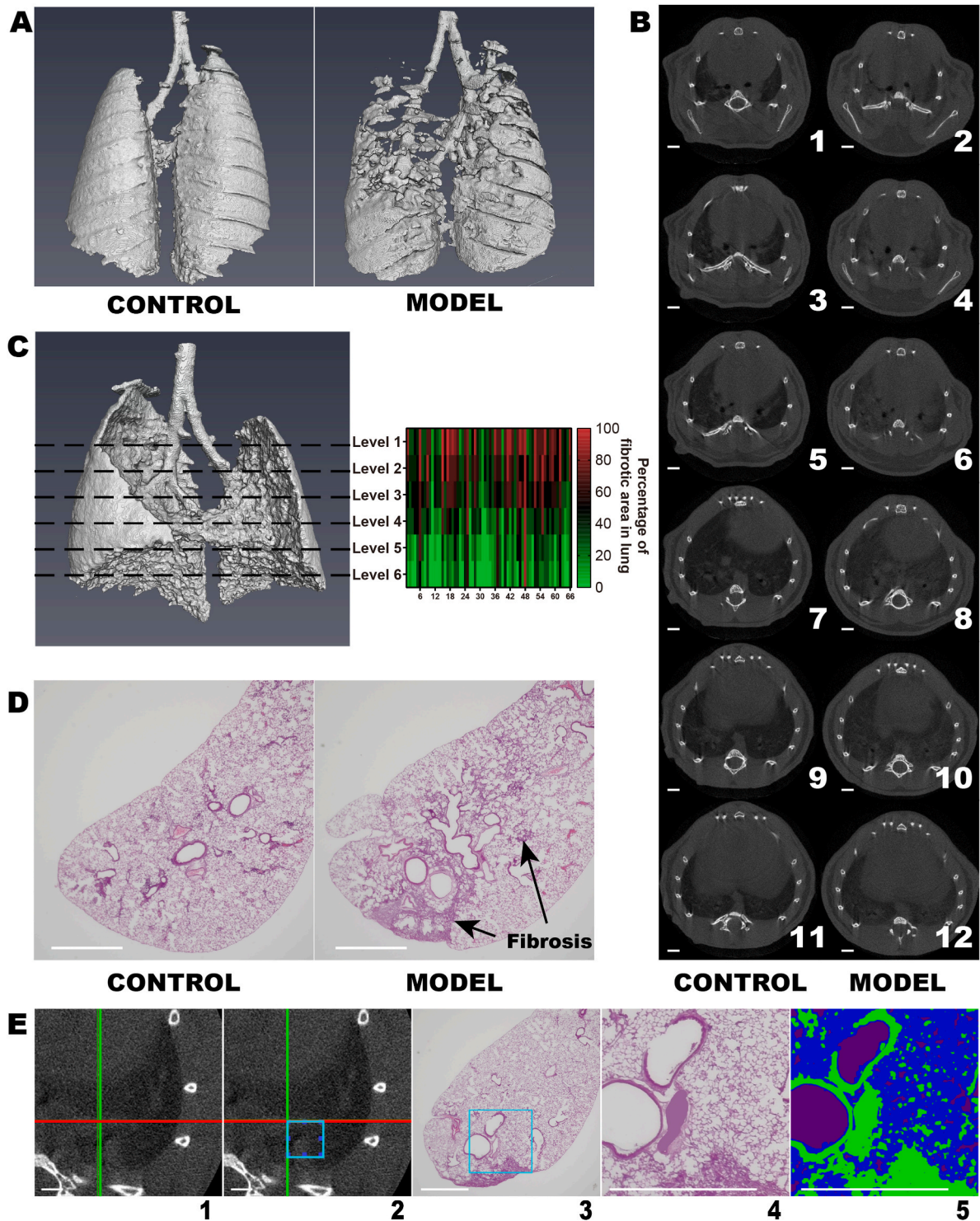
Fig. 2. Characteristics of the bleomycin-induced pulmonary fibrosis mouse model. Representative images of 3D rendering of aerated volume in Control and Model group (**A**). Representative micro-CT images of mouse lungs at specific anatomical levels (**B**): the entrance of cranial right main bronchus (RMB) (Level 1: **B**-1 to 2), the entrance of middle RMB (Level 2: **B**-3 to 4), the entrance of the second branch to left main bronchus (Level 3: **B**-5 to 6), and the maximum area of accessory lobe/diaphragmatic dome (Level 4: **B**-7 to 8), and the lower parts of lung (Level 5: **B**-9 to 10, Level 6: **B**-11 to 12), respectively. The odd numbered images are from the control group and the even numbered images are from the model group. The percentage of fibrotic area from Level 1 to Level 6 was decreased (**C**, n = 66). The representative images exhibited the susceptible site of fibrotic lesion in BIPF mice, with arrowheads indicating the areas of fibrosis (**D**). The workflow of orbit analysis with extraction of ROI corresponding the

VOI in micro-CT (**E**). The process begins with setting the range of VOIC in the left lungs (The red line refers to the sagittal slice; the green line refers to the coronal slice; the cyan box refers to the extracted subvolume box; **E1-2**). HE sections were selected according to the anatomical structure (**E3**). And then, a 700 × 700 pixels (1.278 × 1.278 mm) ROI was extracted from the section corresponding to the range of VOI in the left lungs (**E4**). Finally, the relative proportions of background (aerated area, purple), normal alveoli (blue), and fibrotic and interstitial area (green) in extracted region was analyzed by Orbit (**E5**). White scale bar is 1 mm long. (For interpretation of the references to color in this figure legend, the reader is referred to the Web version of this article.)

(VOIs) are created by taking 100 voxels from each of these points in the lateral, lower, and posterior directions, resulting in VOIs with a side length of 100 voxels. The average percentage of high-density voxels in VOIA/VOIB/VOIC were then calculated to determine the degree of fibrosis in the mouse.

2.6. Whole-lung analysis

To evaluate the percentage of fibrotic area in the whole lung, Whole-lung analysis (WLA) was performed in AVIZO 2019.1 (version 2019.1, Thermofisher, United State). In short, to reduce the level of noise in the original image, a Gaussian filter with an SD [px] of 5*5*5 and kernel size factor of 2 was used to pretreat the image in 3D mode. An aerated area of HU values from -1000 to -737.9 was preliminarily extracted with the magic wand tool, and high-density volumes corresponding to the lung area, such as fibrotic tissues and blood vessels, were added to the same material by the brush tool, delineating the lung area slice by slice manually with interpolation. Areas with HU value above -606.8 were extracted by the threshold segmentation method and added to the other material to obtain a closed extrapulmonary area. Watershed segmentation was used to obtain gradient images and new label fields successively, and then 2-class label fields of the lung and extrapulmonary regions were obtained. Finally, areas of the lung with different densities were segmented to obtain nonaerated (above -672.3 HU value), hypo-aerated ($-737.9 \sim -672.3$ HU value), normo-aerated ($-803.4 \sim -737.9$ HU value), hyperinflated ($-868.8 \sim -803.4$ HU value), and air areas ($-1000 \sim -868.9$ HU value). The percentage of high-density voxels of whole lung was calculated as the percentage of nonaerated volume to the total lung volume.

2.7. Evaluation of pulmonary fibrosis formation by LRA

The study design was shown in Fig. 5A to detect the therapeutic effects of PFD in mice with bleomycin-induced lung injury. Twenty mice were divided into 3 groups: the Control (n = 6), Model (n = 7) and Pirfenidone (PFD, n = 7) groups. The mice in the control group were treated with saline. For the Model and PFD groups, the animals were treated with a single administration of BLM. Seven days later, the mice in the PFD group were gavaged with pirfenidone daily for two weeks, while mice in the Control and Model groups were administered vehicle. All mice were scanned micro-CT imaging at Days 7 and 21 post BLM administration, then sacrificed.

2.8. Evaluation of pulmonary fibrosis resolution by LRA

Previous studies have shown that body weight was negatively correlated with lung tissue weight after induction with bleomycin [11]. Sixteen mice were divided into 2 groups: the Control (n = 6) and Model (BLM, n = 10) groups. The mice in the control group were treated with saline. The mice in the Model group were treated with a single administration of BLM. All mice were undergone micro-CT imaging on Day 21, 42 and 56 post-BLM induction, and then sacrificed. Two mice in the Model group were withdrawn due to over-anesthesia during the scan on Day 42, and another one was withdrawn due to unsuccessful model induction on Day 21.

2.9. Comparison of WLA and LRA

The linear regression analysis was applied to compare the percentage of high-density voxels using WLA or LRA. To assess the robustness of LRA, the linear regression analysis was applied to compare the alterations of LRA in different time points (Day 7 and Day 21) to WLA, respectively. Furthermore, the analysis procedures for both WLA and LRA were performed in triplicate to ensure accuracy and reproducibility.

The consuming time of WLA and LRA analysis were collected from the analysis tool. To identify the minimum sample size for LRA, the goodness-of-fit of different number of samples was conducted. Linear regression analysis between LRA and WLA was applied with the randomized order of samples and increasing the size of samples from 1 to 40. Such a randomization was performed with 15 replicates, resulting in a dataset of goodness-of-fit of LRA to WLA with different sample numbers.

2.10. Histological analysis

After sacrifice, the lungs were harvested. Lungs were inflated with a cannula through the trachea by infusion of 4% para-formaldehyde and fixed for 24 h. Then, the samples were dehydrated in a graded ethanol series and embedded in paraffin. Then five micrometer-thick slices were obtained and used for HE staining. The 20× magnification image of HE sections is acquired by the stereo microscope (Stemi 508, Zeiss). The area of blood vessel was filled with the color of blood vessel wall before Orbit image analysis, because vessel was non-aerated tissue in micro-CT. By Avizo 2019.1, a region of interest (ROI) with 700 × 700 pixels (1.278 × 1.278 mm) were extracted according to the relative position of VOIC in the left lung in each HE section, where was in the lung dorsal segment.
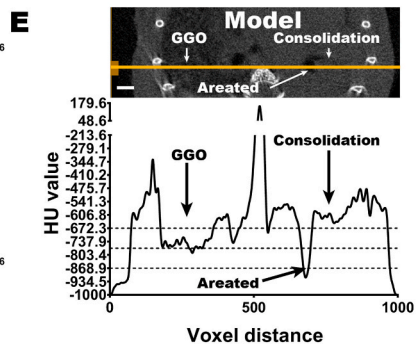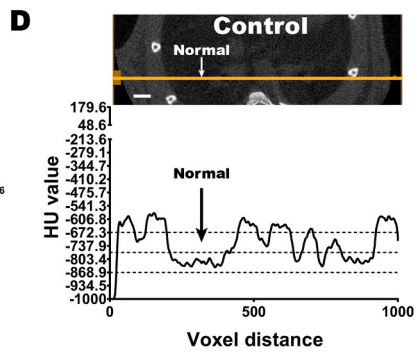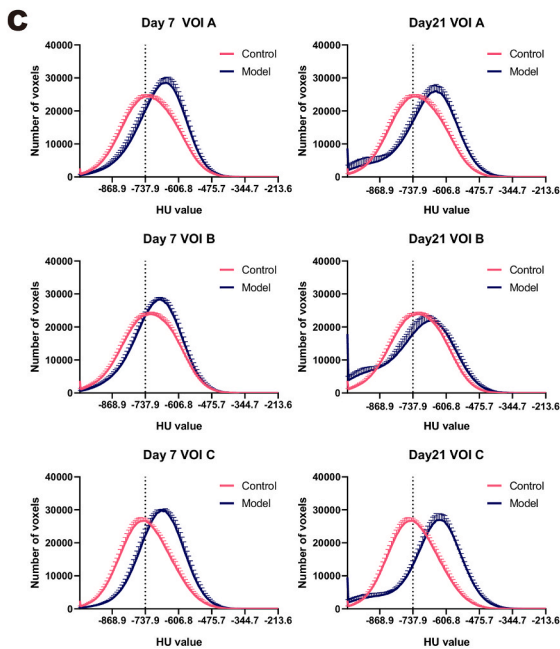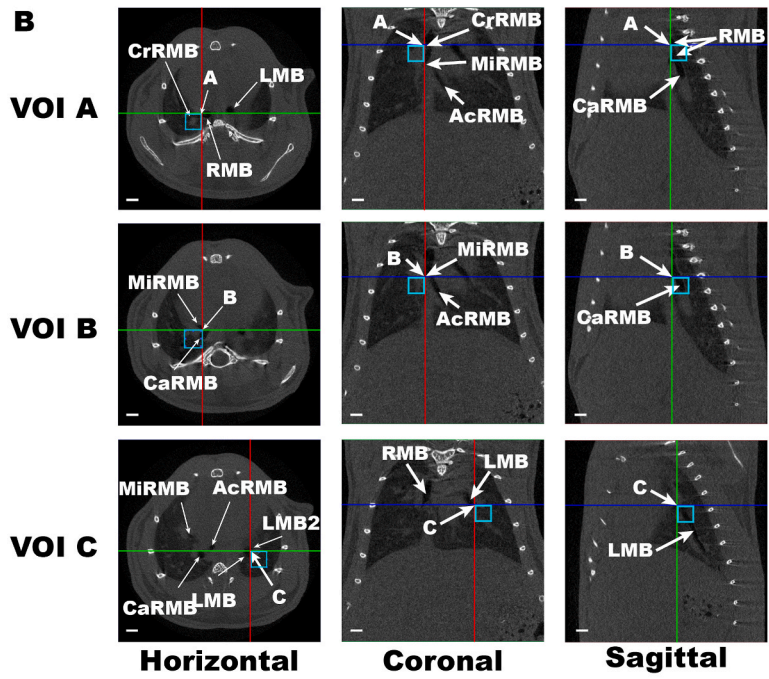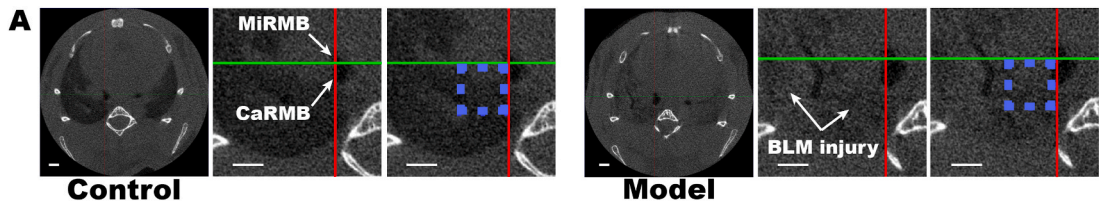
(caption on next page)

Fig. 3. Method development. Subvolume extraction in LRA. Bronchial bifurcation is an obvious marker both in Control and Model groups (**A**). VOIA, VOIB and VOIC were shown from the top, front, and side views, respectively (**B**). The red line refers to the sagittal slice, the green line refers to the coronal slice, the blue line refers to the horizontal slice, and the blue or cyan box is the extracted subvolume box in Figure **A-B**. In the histogram of VOIs in at Day 7 and Day 21, the peak value of the VOIA, B and C of the Model group switch to right comparing to the control group (**C**, n = 6, mean ± SEM). The HU value of the representative sections of Control and Model group was detected by the yellow line probe showed on the right, showing the typical kind of tissue, such as muscle, normal alveoli, hypoaerated alveoli, blood vessel, fibrotic lung, and bone (**D, E**). White scale bar is 1 mm long. (For interpretation of the references to color in this figure legend, the reader is referred to the Web version of this article.)

For each individual, we selected one horizontal section that was around the bifurcation between left main bronchus (LMB) and the second left branch bronchus within VOIC. After that, a classification analysis was performed by Orbit (Orbit image analysis, version 3.64). To assess the correlation between micro-CT and pathology in the stage of established fibrosis (Day 21, Step 2 experiment) and the late stage of fibrosis resolution (Day 56, Step 3 experiment), we harvested the lungs routinely after micro-CT imaging on Day 21 and Day 56.

The Pearson's correlation and univariate linear regression were performed between the percentage of high-density voxels in VOIC and the percentage of fibrotic and interstitial area of ROI. The univariate linear regression was also performed between the percentage of fibrotic and interstitial area of ROI and that of left lung. The percentage of fibrotic and interstitial area of left lung was the mean of percentage in three levels of left lung in one HE section.

2.11. Biochemical quantification of hydroxyproline

The hydroxyproline content of the right upper lobe was determined using a commercial kit (Cat: A030-2-1, Njjcbio, China) according to the manufacturer's protocol. Briefly, the right upper lobe was broken in PBS up to 200 μl. Half of the lysis buffer was hydrolyzed in 1 ml lysing buffer for 20min at 100 °C. Then we adjusted the PH value of sample to 6.0–6.8 and took 200 μl of the reaction buffer to 800 μl ddH2O, and adsorbed insoluble matter with active carbon. Finally, hydroxyproline concentration was determined by the reaction of oxidized hydroxyproline with 4-(Dimethylamino) benzaldehyde (DMAB), which resulted in a colorimetric (560 nm) product, proportional to the hydroxyproline present. The total amount of hydroxyproline was calculated on the right upper lobes.

2.12. Statistical analysis

Data were expressed as the mean and standard error of the mean (SEM) unless otherwise specified. All data and figures were analyzed and created by using GraphPad Prism (version 8.0, GraphPad Software, San Diego CA, United States). One-way ANOVA was applied to find differences between the groups, followed by post hoc analysis and Bonferroni's multiple comparisons test. The two-tailed Mann–Whitney test was used to compare the variance between groups. Univariate linear regression and Pearson correlation analysis were used to assess the relationship between the percentage of high-density voxels in the VOI (volume of interest) and other variables and to determine the accuracy, robustness, and minimal sample size of the LRA. A two-way ANOVA was applied to determine whether there is a statistically significant difference between the means of three or more independent groups that have been split on two variables. The normality and lognormality tests were applied before *t*-test, and Wilcoxon matched-pairs signed rank test or paired *t*-test was used to compare the variance between groups. Welch *t*-test was applied when the data was not normal distribution.

The Pearson's correlation and univariate linear regression were performed between the percentage of high-density voxels in VOIC and the percentage of fibrotic and interstitial area of ROI. The univariate linear regression was also performed between the percentage of fibrotic and interstitial area of ROI and that of left lung. The percentage of fibrotic and interstitial area of left lung was the mean of percentage in three levels of left lung in one HE section.

3. Results

The workflow of this study was showed in Fig. 1, in which three parts are involved: process of method optimization (Fig. 1, Part 1), protocol for evaluating pulmonary fibrosis formation by LRA (Fig. 1, Part 2) and for assessing fibrosis resolution by LRA (Fig. 1, Part 3).

3.1. Part 1: method optimization

3.1.1. Characteristics of the bleomycin induced animal model

To investigate the distribution rule of pulmonary fibrosis lesions and the susceptible sites in BLM-induced pulmonary fibrosis (BIPF) mice, a total of 66 model mice were scanned at Day 21 post-instillation. Our micro-CT data showed that the 65 fibrotic lesions in 66 BLM induced mice were mainly distributed in the mid-to upper-lung 21 days after BLM administration (Fig. 2A–C). In addition, the characteristic feature of BIPF mice model was hypostatic pneumonia that usually resulted from the collection of fluid in the dorsal region of the lungs (Fig. 2D). We compared the characteristics of the lung injury by using micro-CT and histopathology examination. As was shown in Fig. 2E, the location of the fibrosis lesion was consistent both in radiological and pathological results.

3.1.2. Establishment of longitudinal and regional analysis (LRA)

Fig. 3A showed the micro-CT slice of the bronchial bifurcation where RMB splits into the MiRMB. This location could clearly reveal
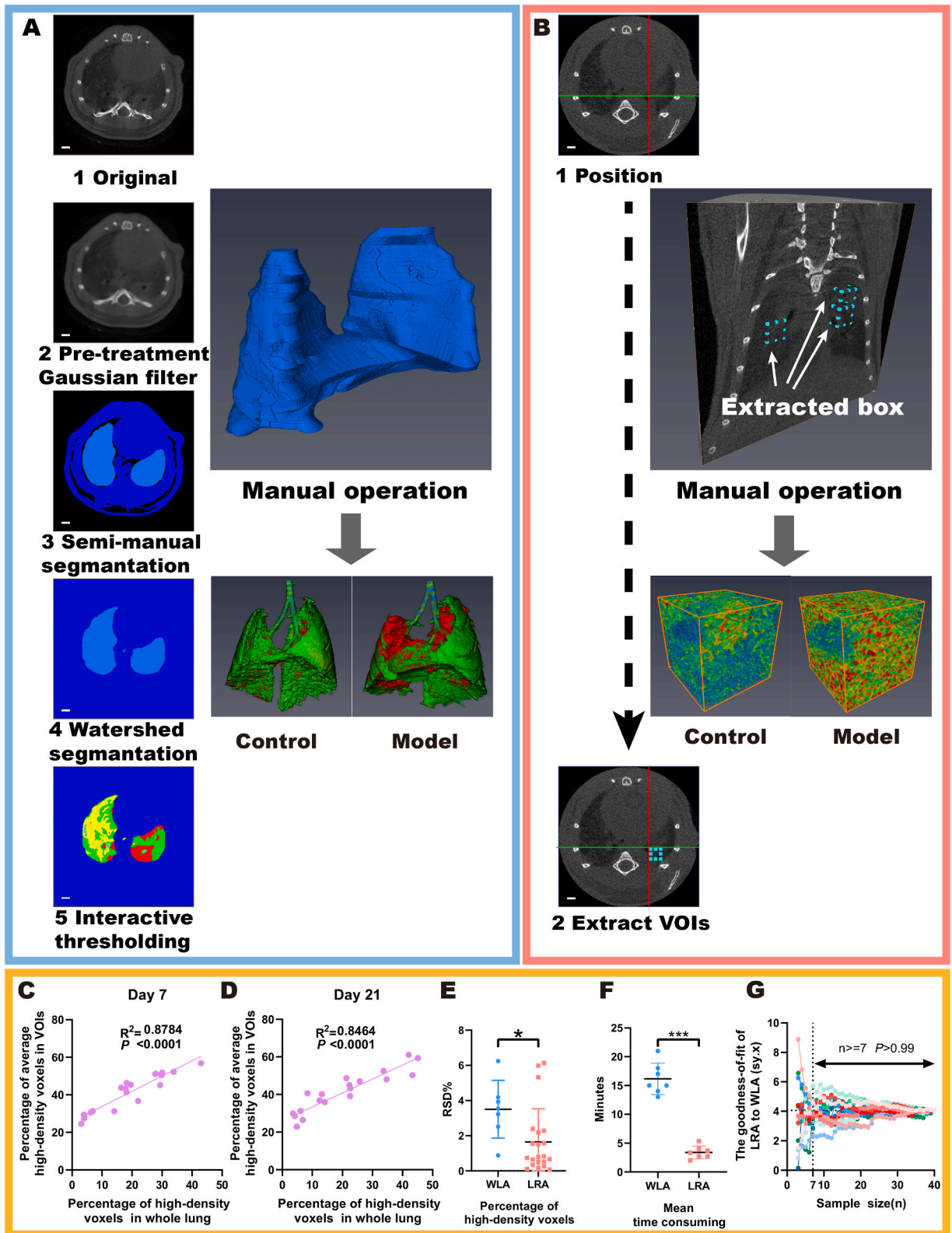
(caption on next page)

Fig. 4. Comparison of whole-lung analysis and Longitudinal and regional analysis. The *top left panel* described the workflow for the percentage of high-density voxels in whole lung analysis (**A**). Briefly, the process began with noise reduction by Gaussian filter (**A1-2**). The material, the area of lung, was manually delineated by brush tool levels by level following with interpolation. After locking the lung material, a higher density extrapulmonary area was determined by interactive thresholding (**A3**). Watershed segmentation was used to obtain the dichotomy label fields of lung and extrapulmonary region (**A4**). Further segmentation by different gray value was performed (**A5**). Finally, the density of the lung was segmented to obtain the areas of the non-aerated (red, above −672.3 HU value), the hypo-aerated (green, −737.9 ~ −672.3 HU value), the normo-aerated (yellow, −803.4 ~ −737.9 HU value), and the hyper-inflated (blue, −868.8 ~ −803.4 HU value). The *top right panel* described the workflow of LRA (**B**). Briefly, the process involved setting position of VOIs and performing histogram analysis. The representative subvolumes were showed in physics.iol colormap, that there is non-aerated (red), hypo-aerated (yellow), normo-aerated (green-cyan), and air (blue). The *bottom panel* described the accuracy and robustness of LRA. The correlation between the percentage of high-density voxels in WLA and LRA was $R^2 = 0.8784$ and 0.8464 at Day 7 and Day 21, respectively (**C, D**). The RSD of the percentage of high-density voxels in LRA was significantly less than that in WLA (1.645 ± 1.884% VS 3.501 ± 1.637%, $P = 0.0282$, **E**). The mean time of analysis of WLA and LRA ($P < 0.001$, n = 7, **F**). The goodness-of-fit between LRA and WLA trended to stabilize with an increasing number of sample sizes (**G**). (For interpretation of the references to color in this figure legend, the reader is referred to the Web version of this article.)

the occlusion of normal condition and lung consolidation after BLM injury. Fig. 3B showed the location of VOIA, VOIB and VOIC with the annotation of anatomical structure from the top, front, and side views. After bleomycin injury, significant alterations were shown in all VOIs between the control group and Model group at Days 7 and 21 (Fig. 3C). In the bleomycin-induced pulmonary fibrosis mouse model, there existed marked ground-glass opacity (GGO) and consolidation (Fig. 3D and E). The density of the lungs reflected the disease degree of pulmonary fibrosis. As shown in Fig. 3D and E, a yellow line was set in each figure to detect the HU value of normal alveoli, GGO, and lung consolidation. Based on the HU values-voxel distance graph, which reduces noise by averaging the HU values of 10 pixels in Fig. 3D and E, it was determined that the variant HU value of normal alveoli ranged from −868.9 to −803.4, while the HU value of GGO was in the range of −868.9 to −737.9. The HU value of consolidation was found to be higher than −672.3 but less than −475.7, and the HU value of bronchus was lower than −868.9. At the same time, the HU value of bones was higher than −213.6. Based on these findings, the HU value range of −868.9 to −803.4 was considered normal for alveoli, while the range of −868.9 to −737.9 was indicative of hyperaerated alveoli. The range of −737.9 to −672.3 was suggestive of normal hypoaerated alveoli, overlapping with small blood vessels and mild fibrotic alveoli (GGO). HU values between −672.3 and −213.6 were reflective of high density, representing typical serious fibrotic tissues. Additionally, the peak HU value of approximately 48.6 in Fig. 3E was attributed to bone tissue.

3.1.3. Comparison LRA with WLA

The protocol of WLA and LRA were shown in Fig. 4A and **B**, respectively. As expected, the percentage of high-density voxels in the VOIs was well correlated with the percentage of high-density voxels obtained by WLA at Day 7 and Day 21 after bleomycin administration (Fig. 4C and **D**; $R^2 = 0.8784$ and $R^2 = 0.8464$, respectively; $P < 0.0001$; Control, n = 6; Model group, n = 7, PFD group, n = 7). Thus, LRA exhibited good accuracy relative to classical WLA and good robustness at different time points in the bleomycin model.

To compare the repeatability of LRA and WLA, the whole-lung volume and the VOIA, VOIB and VOIC were extracted three times from the Model group (n = 7) on Day 7 after BLM administration. The relative standard deviations (RSDs) of the X, Y and Z coordinates of each VOI were 0.000–1.1437%, 0.000–1.1715%, and 0.000–1.2.000%, respectively. Moreover, the RSD of the percentage of high-density voxels in LRA was significantly smaller than that in WLA (Fig. 4E and 1.645 ± 1.884% VS 3.501 ± 1.637%, $P = 0.0282$), indicating that LRA exhibited better repeatability for assessing the percentage of fibrosis in the ROI.

To validate the ability of LRA to speed up analysis of lung fibrosis, we collected the time for conducting WLA and LRA from the analysis tool and compared the differences between the consuming time of WLA and LRA. Results showed that the consuming time of analysis of LRA was significantly shorter than that of WLA (Fig. 4F, $P < 0.001$, n = 7). Additionally, the Pearson correlation was strong between LRA and WLA in the population ($R^2 = 0.856$, $P < 0.0001$, sy.x = 4.05). With the increasing of sample size, the goodness-of-fit of LRA to WLA gradually stabilized at 4.05. When the sample size was equal to or larger than 7, the goodness-of-fit of LRA approached to saturation (Fig. 4G, $P > 0.99$; n = 40).

3.2. Part 2: application of LRA in evaluating pulmonary fibrosis formation

We firstly applied LRA to assess the antifibrotic effect of Pirfenidone (PFD, FDA approved drug) in the BLM-induced mouse model (Fig. 5A). The body weight loss of mice in the PFD-treated group revealed no marked changes with the model group (Fig. 5B, $P > 0.05$, Control group, n = 6; Model group, n = 7; PFD group, n = 7).

Both the Model group and PFD group exhibited significantly increased percentages of high-density voxels in the whole lung at Day 7 by WLA (Fig. 5C, Control vs. Model group, ### $P < 0.001$; Model group vs. PFD group, $P > 0.05$). Moreover, there was no significant difference between Model group and PFD group in the percentage of high-density voxels in the whole lung between Day 7 and Day 21 by using the paired *t*-test (Fig. 5D and, **E**). LRA showed similar results as WLA (Fig. 5F, **G** and **H**).

To verify the accuracy of the micro-CT detection of fibrotic lesions at 21 days after BLM injury, linear regression analysis was applied to determine the correlation between the percentage of high-density voxels of VOIC in LRA and the percentage of fibrotic and interstitial area of ROI in HE sections and good correlations were identified (Fig. 5I, $R^2 = 0.7751$; $P < 0.0001$).

Moreover, there were significant correlations between the percentage of fibrotic and interstitial area of ROI and that of the left lung by applying linear regression analysis (Fig. 5J, $R^2 = 0.7434$; $P < 0.0001$). The fibrotic and interstitial area of the left lung in the HE sections from Orbit analysis of the PFD group were also significantly smaller than those in the Model group (Fig. 5K, $P = 0.0320$).
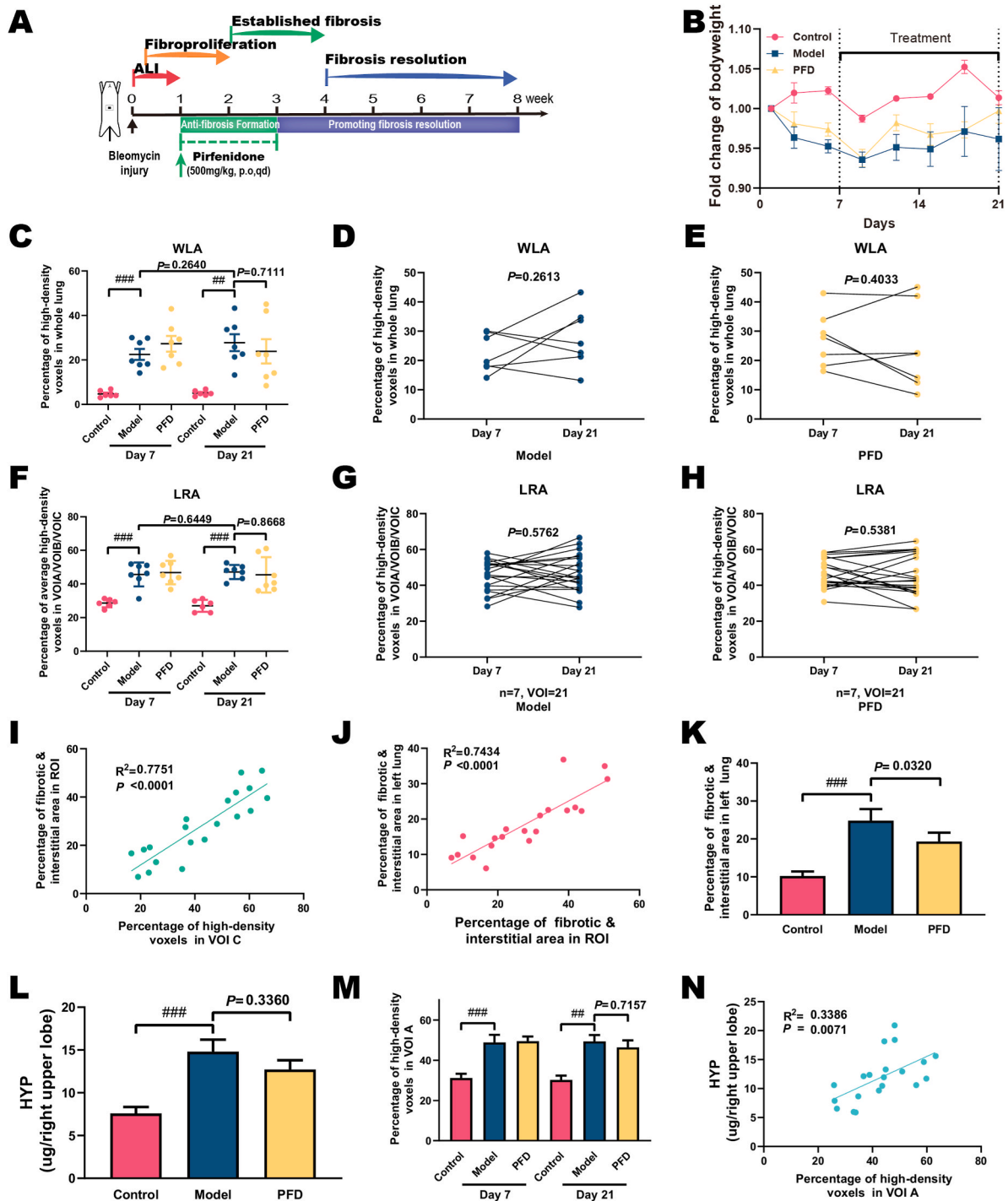
Fig. 5. Application and validation of LRA in evaluating the antifibrotic effect of pirfenidone. Outline of the design of pirfenidone in mice with initial fibrosis following Bleomycin-induced lung injury (**A**). The percentage of body weight change during Day 0 to Day 21 (**B**). The percentage of high-density voxels in WLA at Day 7 and Day 21 related to graph B (**C**, Control vs. Model group, ## $P < 0.01$, ###$P < 0.001$). The percentage of high-density voxels in WLA were compared with Day 7 and Day 21 in Model group (**D**) and PFD group (**E**). The percentage of average high-density voxels in VOIA/VOIB/VOIC in LRA at Day 7 and Day 21 (**F**, Control vs. Model group, ###$P < 0.001$). The percentage of high-density voxels in VOIA/VOIB/VOIC of LRA were compared with Day 7 and Day 21 in Model group (**G**) and PFD group (**H**). Linear regression analysis between the percentage of fibrotic and interstitial area in ROI of the section and the percentage of high-density voxels in VOIC of micro-CT (**I**, $R^2 = 0.7751$, $P < 0.0001$). Linear regression analysis between the percentage of fibrotic and interstitial area in ROI of the section and the percentage of fibrotic and interstitial area in left lung (**J**, $R^2 = 0.7434$, $P < 0.0001$). The percentage of fibrotic and interstitial area in left lung in HE sections from Orbit

analysis (K, Control vs. Model group, $\#\#\#P < 0.001$; Model vs. PFD group, $P = 0.0320$). HYP content in the right upper lobes were determined by commercial kit (**L**, Control vs. Model group, $\#\#\#P < 0.001$; Model vs. PFD group, $P = 0.3360$). The percentage of high-density voxels in VOIA at Day 7 and Day 21 (**M**, Control vs. Model group, $\#\#P < 0.01$, $\#\#\#P < 0.001$; Model vs. PFD group, $P > 0.05$). Linear regression analysis between HYP content with the percentage of high-density in VOIA at Day 21(**N**, $R^2 = 0.3386$, $P = 0.0071$). Data presented as mean $\pm$ SEM; Control group, n = 6; Model group, n = 7; PFD group, n = 7. Data were analyzed by using unpaired t-test, one-way ANOVA or linear regression analysis. Figure **D**, **E**, **G**, and **H** were analyzed by using paired t-test.

The hydroxyproline (HYP) content of the right upper lobe were significantly increased in the Model group compared to the control group, while PFD decreased the HYP level comparing to the Model group (Fig. 5L, $P = 0.3360$). Since we measured the HYP level of the right upper lobe, the linear regression analysis was performed between HYP and VOIA which was located on the right upper lobe. The percentage of high-density voxels in VOIA was significantly increased in the Model and PFD groups compared to the control group at Day 7 (Fig. 5M, $P < 0.05$) and was not significantly different between the BLM and PFD groups (Fig. 5M, $P > 0.05$). On Day 21, the percentage of high-density voxels in VOIA in the PFD group was slightly reduced compared to that in the BLM group ($P = 0.7157$). To evaluate the relationship between LRA and HYP at 21 days after bleomycin induction, a linear regression analysis was performed and results showed a little correlation between the percentage of high-density voxels in VOIA and the HYP content of the right upper lobe (Fig. 5N, $R^2 = 0.3386$, $P = 0.0071$).

3.3. Part 3: application of LRA in evaluating pulmonary fibrosis resolution

As shown in Fig. 6A, the body weights of mice in the model group were lower than that of the control group after BLM injury (n_{model} = 7, $n_{control}$ = 6). The percentage of high-density voxels in the VOIs was significantly increased at Day 21 and then improved a little at Day 56 (Fig. 6B, Day 21, $P < 0.01$; Day 56, $P = 0.3365$; n_{model} = 7, $n_{control}$ = 6). The percentage of high-density voxels in VOIA/VOIB/ VOIC in survival mice showed that bleomycin-treated mice developed pulmonary fibrosis resolution from Day 21–56 after instillation (Fig. 6C, $P < 0.01$, n_{VOI} = 21). Since we detected the histological change on the left lung and the HYP level of the right upper lobe, the linear regression analysis was performed between the ROI of HE sections and VOIC and between HYP and VOIA respectively, to assess the accuracy of micro-CT in detecting fibrotic lesions at 56 days after BLM injury. The results showed there were good correlations between the percentage of fibrotic and interstitial area in the ROI of HE sections and the percentage of high-density voxels in VOIC of LRA (Fig. 6D, $R^2 = 0.8321$; $P < 0.0001$, n = 13), as well as the moderate correlations between the HYP content of the right upper lobe and the percentage of high-density voxels in VOIA (Fig. 6E, $R^2 = 0.6117$; $P = 0.0377$, n = 7).

4. Discussion

Micro-CT imaging is widely utilized to evaluate the efficacy of potential anti-fibrosis drugs in preclinical models [12]. A large number of mice are applied to deliver reliable data in a short time to identify the best anti-fibrosis drug candidates; however, an easier, time-saving strategy of micro-CT in fibrosis drug discovery is still lacking. In this study, we established LRA to evaluate fibrosis in a murine model of BLM-induced lung fibrosis, which took less time but has the comparable capacity to reflect fibrosis to WLA and histological examination.

Through the semi-quantification of micro-CT images obtained from 66 mice, we observed that the distribution pattern of fibrosis was predominantly located in the mid-to upper- and dorso-centric regions of the lungs 21 days after bleomycin administration, consistent with prior published studies [4–6,8,13–17]. This distribution pattern may be attributable to the fact that bleomycin primarily settles in the mid-to upper-lungs along with the airflow of breathing. Our findings suggest that imaging changes in volume of interests (VOIs) in these regions can effectively reflect the progression of pulmonary fibrosis. Moreover, the utilization of LRA markedly improved the speed of analysis, thereby making it a superior option for studies with large sample sizes of mice in anti-fibrosis drug discovery research.

The search for drugs capable of reversing established fibrosis is a burgeoning field of research that necessitates suitable methods for longitudinal assessment [18,19]. In the long-term observation of study, few disease indictors have been performed to evaluate the disease stage of BLM-induced fibrosis and determine the optimal timing of anti-fibrosis drug candidate treatment prior to animal sacrifice. Classical endpoint indicators, such as ASMA, type 1 collagen, Ashcroft scoring and endpoint micro-CT, may only reflect the disease stage on the day of sacrifice [16]. Micro-CT imaging is a noninvasive choice for process evaluation. The newly established LRA is likely to be a rapid and easy method to reflect the different disease stage of fibrosis. Using LRA analysis, we detected an increase in lung density after fibrosis developed at Day 21 post-bleomycin injury, and a reduction of lung density at Day 56 post-bleomycin injury. Furthermore, the accuracy of LRA was further confirmed by the histological analysis and biochemical quantification of hydroxy-proline, supporting the usefulness of LRA as a process indicator for assessing disease stage.

Although LRA is likely an easier and more time-saving method to assess fibrosis using micro-CT, it has been observed that its sensitivity is relatively lower compared to WLA. As such, this approach is more appropriate to be applied in mice experiments with larger sample sizes. Since LRA is a sampling method used for the uneven but regular distribution of lesions, having a small number of samples may result in small numbers error, which can impact the accuracy of the data. Therefore, we plan to use a larger number of animals to further validate the validity of the LRA method. Furthermore, it is important to note that LRA can only analyze the area within the VOIA/VOIB/VOIC, and therefore may not provide information about total lung volume or other areas outside the extracted box. It is also worth mentioning that LRA may not detect the effects of potential drugs that act on functional alveoli rather than on
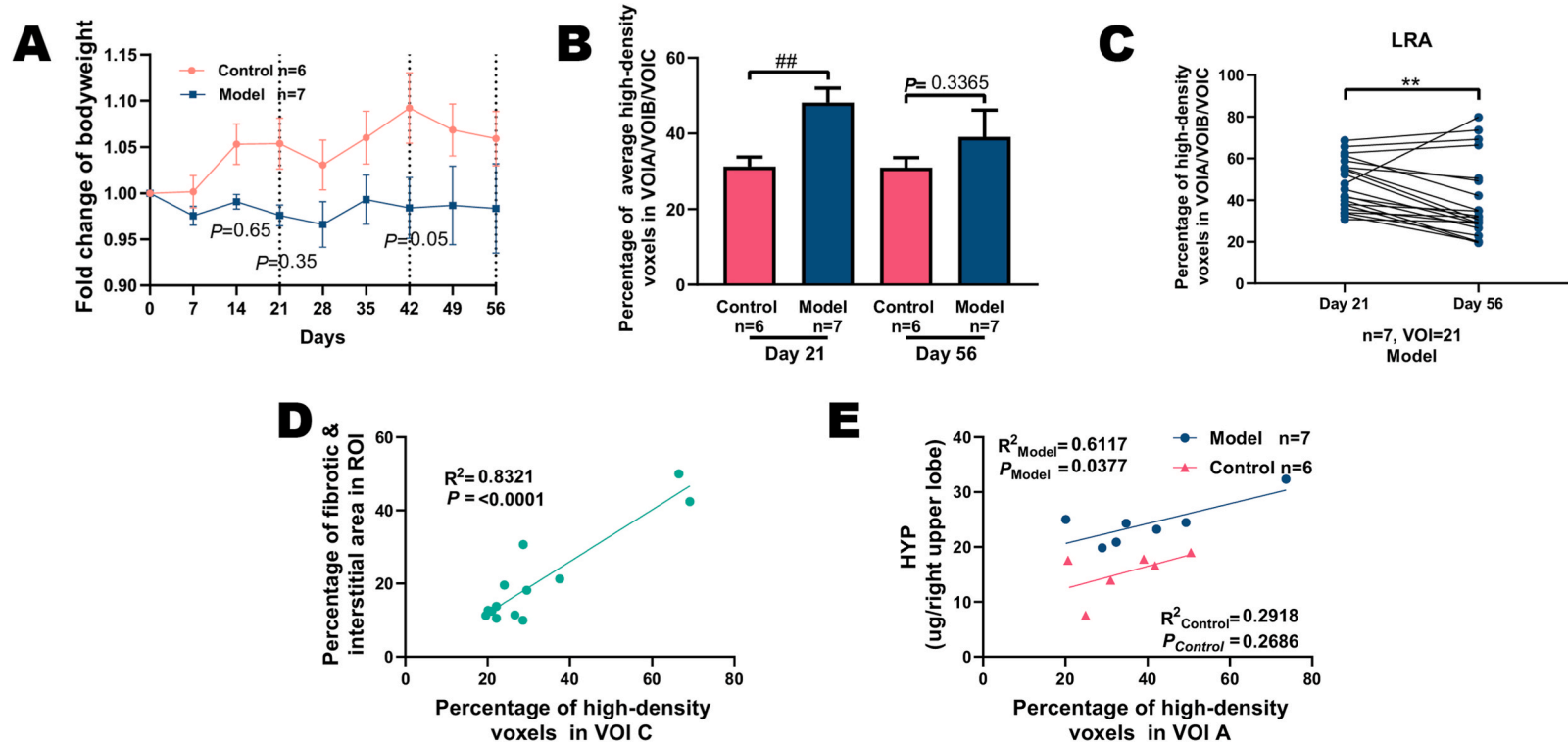
Fig. 6. Application of LRA in evaluating pulmonary fibrosis resolution. The percentage of body weight change from Day 0 to Day 56 (**A**). The percentage of average high-density voxels in VOIA/VOIB/VOIC in LRA between Control and Model groups at Day 21 and Day 56, respectively (**B**, Control vs. Model group, #$P < 0.05$, Day 21: $n_{Control} = 6$, $n_{Model} = 10$; Day 56: $n_{Control} = 6$, $n_{Model} = 7$). The percentage of average high-density voxels in VOIA/VOIB/VOIC of LRA were compared between Day 21 and Day 56 in Model group (**C**, $P < 0.01$, n = 7, $n_{VOI} = 21$). Linear regression analysis between the percentage of fibrotic and interstitial area in ROI with the percentage of high-density voxels in VOIC at Day 56 (**D**, $R^2 = 0.8321$, $P < 0.0001$, n = 13). Linear regression analysis between HYP content of right upper lobe with the percentage of high-density voxels in VOIA at Day 56 (**E**, $n_{Model} = 7$, $R^2_{Model} = 0.6117$, $P_{Model} = 0.0377$). Data presented as mean ± SEM. Data were analyzed by using unpaired t-test and linear regression. Figure **C** were analyzed by using Wilcoxon matched-pairs signed rank test.

deposited collagen. Finally, the unexpected development of bronchiectasis or bronchial occlusion in the bronchus of BIPF may alter the proportion of the bronchus in the VOI. Experiences with large sample sizes were suggested for further validations.

5. Conclusion

LRA was a faster and easier micro-CT quantification method designed to evaluate regional changes in pulmonary fibrosis before and after treatment. The applications of LRA may open the way to assess the disease stage of fibrosis and anti-fibrosis drug evaluation in a longitudinal observation.

Author contribution statement

Ruogu Lai: Conceived and designed the experiments; Performed the experiments; Analyzed and interpreted the data; Contributed reagents, materials, analysis tools or data; Wrote the paper.

Caiping Zhao, Wanyi Guo, Yao Xiao, and Runze Li: Performed the experiments; Contributed reagents, materials, analysis tools or data.

Liang Liu: Conceived and designed the experiments; Contributed reagents, materials, analysis tools or data.

Hudan Pan: Conceived and designed the experiments; Analyzed and interpreted the data; Contributed reagents, materials, analysis tools or data; Wrote the paper.

Data availability statement

Data will be made available on request.

Declaration of interest's statement

The authors declare no conflict of interest.

Additional information

No additional information is available for this paper.

Availability of data and materials

The datasets during and/or analyzed during the current study available from the corresponding author on reasonable request.

Ethics approval and consent to participate

All procedures were approved by the Animal Ethical Council of Macau university of science and technology.

Consent for publication

This manuscript does not contain any individual person's data.

Declaration of competing interest

The authors declare that they have no known competing financial interests or personal relationships that could have appeared to influence the work reported in this paper.

Acknowledgments

References

[1] G. Raghu, Diagnosis of idiopathic pulmonary fibrosis. An official ATS/ERS/JRS/ALAT clinical practice guideline, Am. J. Respir. Crit. Care Med. 198 (2018) e44–e68, https://doi.org/10.1164/rccm.201807-1255ST.

[2] G. Raghu, H.R. Collard, J.J. Egan, F.J. Martinez, J. Behr, K.K. Brown, T.V. Colby, J.F. Cordier, K.R. Flaherty, J.A. Lasky, D.A. Lynch, J.H. Ryu, J.J. Swigris, A. U. Wells, J. Ancochea, D. Bouros, C. Carvalho, U. Costabel, M. Ebina, D.M. Hansell, T. Johkoh, D.S. Kim, T.E. King Jr., Y. Kondoh, J. Myers, N.L. Müller, A. G. Nicholson, L. Richeldi, M. Selman, R.F. Dudden, B.S. Griss, S.L. Protzko, H.J. Schünemann, An official ATS/ERS/JRS/ALAT statement: idiopathic pulmonary

fibrosis: evidence-based guidelines for diagnosis and management, Am. J. Respir. Crit. Care Med. 183 (2011) 788–824, https://doi.org/10.1164/rccm.2009-040GL.

[3] T. Liu, F.G. De Los Santos, S.H. Phan, The bleomycin model of pulmonary fibrosis, Methods Mol. Biol. 1627 (2017) 27–42, https://doi.org/10.1007/978-1-4939-7113-8_2.

[4] H.J. Lee, J.M. Goo, N.R. Kim, M.A. Kim, D.H. Chung, K.R. Son, H.C. Kim, C.H. Lee, C.M. Park, E.J. Chun, J.G. Im, Semiquantitative measurement of murine bleomycin-induced lung fibrosis in in vivo and postmortem conditions using microcomputed tomography: correlation with pathologic scores–initial results, Invest. Radiol. 43 (2008) 453–460, https://doi.org/10.1097/RLI.0b013e31816900ec.

[5] A. Arora, V. Bhuria, P.P. Hazari, U. Pathak, S. Mathur, B.G. Roy, R. Sandhir, R. Soni, B.S. Dwarakanath, A.N. Bhatt, Amifostine analog, DRDE-30, attenuates bleomycin-induced pulmonary fibrosis in mice, Front. Pharmacol. 9 (2018) 394, https://doi.org/10.3389/fphar.2018.00394.

[6] E. Ferrini, L. Mecozzi, L. Corsi, L. Ragionieri, G. Donofrio, F.F. Stellari, Alfaxalone and dexmedetomidine as an alternative to gas anesthesia for micro-CT lung imaging in a bleomycin-induced pulmonary fibrosis murine model, Front. Vet. Sci. 7 (2020), 588592, https://doi.org/10.3389/fvets.2020.588592.

[7] H. Kim, S.H. Park, S.Y. Han, Y.S. Lee, LXA(4)-FPR2 signaling regulates radiation-induced pulmonary fibrosis via crosstalk with TGF-β/Smad signaling, Cell Death Dis. 11 (2020) 653, https://doi.org/10.1038/s41419-020-02846-7.

[8] Z. Xue, F. Zhao, X. Sang, Y. Qiao, R. Shao, Y. Wang, S. Gao, G. Fan, Y. Zhu, J. Yang, Combination therapy of tanshinone IIA and puerarin for pulmonary fibrosis via targeting IL6-JAK2-STAT3/STAT1 signaling pathways, Phytother. Res. 35 (2021) 5883–5898, https://doi.org/10.1002/ptr.7253.

[9] R.G. Jenkins, B.B. Moore, An official american thoracic society workshop report: use of animal models for the preclinical assessment of potential therapies for pulmonary fibrosis, Am. J. Respir. Cell Mol. Biol. 56 (2017) 667–679, https://doi.org/10.1165/rcmb.2017-0096ST.

[10] L. Mecozzi, M. Mambrini, F. Ruscitti, E. Ferrini, R. Ciccimarra, F. Ravanetti, N. Sverzellati, M. Silva, L. Ruffini, S. Belenkov, M. Civelli, G. Villetti, F.F. Stellari, *In-vivo* lung fibrosis staging in a bleomycin-mouse model: a new micro-CT guided densitometric approach, Sci. Rep. 10 (2020), 18735, https://doi.org/10.1038/s41598-020-71293-3.

[11] P.M. Cowley, C.R. Roberts, A.J. Baker, Monitoring the health status of mice with bleomycin-induced lung injury by using body condition scoring, Comp. Med. 69 (2019) 95–102, https://doi.org/10.30802/AALAS-CM-18-000060.

[12] G. Vande Velde, J. Poelmans, E. De Langhe, A. Hillen, J. Vanoirbeek, U. Himmelreich, R.J. Lories, Longitudinal micro-CT provides biomarkers of lung disease that can be used to assess the effect of therapy in preclinical mouse models, and reveal compensatory changes in lung volume, Dis. Model Mech. 9 (2016) 91–98, https://doi.org/10.1242/dmm.020321.

[13] G.Y. Jin, S.M. Bok, Y.M. Han, M.J. Chung, K.H. Yoon, S.R. Kim, Y.C. Lee, Effectiveness of rosiglitazone on bleomycin-induced lung fibrosis: assessed by micro-computed tomography and pathologic scores, Eur. J. Radiol. 81 (2012) 1901–1906, https://doi.org/10.1016/j.ejrad.2010.12.061.

[14] E. De Langhe, G. Vande Velde, J. Hostens, U. Himmelreich, B. Nemery, F.P. Luyten, J. Vanoirbeek, R.J. Lories, Quantification of lung fibrosis and emphysema in mice using automated micro-computed tomography, PLoS One 7 (2012), e43123, https://doi.org/10.1371/journal.pone.0043123.

[15] A. Blandinieres, T. Gille, J. Sadoine, I. Bieche, L. Slimani, B. Dizier, P. Gaussem, C. Chaussain, C. Planes, P. Dorfmuller, D. Israel-Biet, D.M. Smadja, Endothelial colony-forming cells do not participate to fibrogenesis in a bleomycin-induced pulmonary fibrosis model in nude mice, Stem Cell Rev. Rep. 14 (2018) 812–822, https://doi.org/10.1007/s12015-018-9846-5.

[16] S. Song, Z. Fu, R. Guan, J. Zhao, P. Yang, Y. Li, H. Yin, Y. Lai, G. Gong, S. Zhao, J. Yu, X. Peng, Y. He, Y. Luo, N. Zhong, J. Su, Intracellular hydroxyproline imprinting following resolution of bleomycin-induced pulmonary fibrosis, Eur. Respir. J. 59 (2022), https://doi.org/10.1183/13993003.00864-2021.

[17] K. Dekoster, T. Decaesteker, N. Berghen, S. Van den Broucke, A.C. Jonckheere, J. Wouters, A. Krouglov, R. Lories, E. De Langhe, P. Hoet, E. Verbeken, J. Vanoirbeek, G. Vande Velde, Longitudinal micro-computed tomography-derived biomarkers quantify non-resolving lung fibrosis in a silicosis mouse model, Sci. Rep. 10 (2020), 16181, https://doi.org/10.1038/s41598-020-73056-6.

[18] E. El Agha, A. Moiseenko, V. Kheirollahi, S. De Langhe, S. Crnkovic, G. Kwapiszewska, M. Szibor, D. Kosanovic, F. Schwind, R.T. Schermuly, I. Henneke, B. MacKenzie, J. Quantius, S. Herold, A. Ntokou, K. Ahlbrecht, T. Braun, R.E. Morty, A. Gunther, W. Seeger, S. Bellusci, Two-way conversion between lipogenic and myogenic fibroblastic phenotypes marks the progression and resolution of lung fibrosis, Cell Stem Cell 20 (2017) 261–273 e3, https://doi.org/10.1016/j.stem.2016.10.004.

[19] S. Rangarajan, N.B. Bone, A.A. Zmijewska, S. Jiang, Metformin reverses established lung fibrosis in a bleomycin model, Nat. Med. 24 (2018) 1121–1127, https://doi.org/10.1038/s41591-018-0087-6.